Journal of Atmospheric and Solar-Terrestrial Physics 71 (2009) 697–707

Contents lists available at ScienceDirect

Journal of
Atmospheric and Solar-Terrestrial Physics

journal homepage: www.elsevier.com/locate/jastp

Assessing auroral electric field variance with coherent and incoherent scatter radar

D.L. Hysell [a,*], G. Michhue [a], M.J. Nicolls [b], C.J. Heinselman [b], M.F. Larsen [c]

[a] Earth and Atmospheric Sciences, Cornell University, Ithaca, NY, USA
[b] SRI International, Menlo Park, CA, USA
[c] Department of Physics, Clemson University, Clemson, SC, USA

ARTICLE INFO

Article history:
Accepted 14 October 2008
Available online 11 December 2008

Keywords:
Aurora
Electric fields
Radar
Farley Buneman instability

ABSTRACT

Line-of-sight *F* region plasma drifts measured with the Poker Flat Incoherent Scatter Radar (PFISR) during the NASA JOULE II experiment period are compared with estimates derived from *E* region coherent scatter spectra observed with a 30 MHz imaging radar on common magnetic field lines. The estimates are based on empirical formulas determined through earlier comparisons between in situ and ground-based measurements. Good agreement is found in the current study when the radar measurements are sufficiently well collocated and the convection is sufficiently homogeneous for meaningful comparison. The mean and variance of the background electric field are also estimated from the coherent scatter data and used to assess the contribution of fine structure in the convection pattern to Joule heating. Fine structure in the scale size regime between ~2 and 200 km is found to increase the second moment of the electric field by up to 50% for intervals of a few minutes during a substorm when the flow was highly irregular. The average contribution to the net Joule heating rate is generally likely to be modest, however.

1. Introduction

The NASA JOULE II sounding rocket experiment was conducted in Alaska in January 2007, to evaluate the contribution of fine structure in the auroral convection electric field to Joule heating, which depends quadratically on the electric field and is susceptible to underestimation if fine structure is neglected (Codrescu et al., 1995, 2000; Li et al., 1998). Electric fields were measured with three instruments sensitive to flow features over a broad range of spatial and temporal scales. The Poker Flat Incoherent Scatter Radar (PFISR) measured the regional convection pattern with a spatial resolution of several tens of kilometers. A coherent scatter radar imager located in Anchorage observed plasma waves in the auroral electrojet with a spatial resolution of a few kilometers. Echoes from the irregularities appear to be telltales of the convection electric field mapped into the *E* region. Instrumented sounding rockets launched from the Poker Flat Rocket Range (PFRR) made point measurements of the vector electric field along their trajectories.

Some preliminary experimental results were described by Hysell et al. (2008) who focused on relating the coherent scatter data to the background electric fields observed by rockets. The rocket measurements were mapped along geomagnetic field lines to the *E* region scattering volume and compared with the Doppler spectra of echoes arising from that volume. Confirming the results of Bahcivan et al. (2005) and Hysell et al. (2008) found empirical relationships between the moments of the spectra (Doppler shifts, spectral widths) and the corresponding line-of-sight and cross-track components of the electron drift velocity. Using these empirical formulas, they were able to predict the spectral moments on the basis of the electric fields measured in situ. It should be noted that the formulas in question had little theoretical justification at first but now appear to be consistent with recent numerical simulations of Farley Buneman waves (Oppenheim et al., 2008).

The empirical formulas in question imply a means of inverting the coherent scatter radar spectra and estimating vector electric fields from single-station data. In this paper, such inversions are attempted. Electric fields are inferred from the coherent scatter data and mapped along geomagnetic field lines into the scattering volume(s) of the PFISR. Comparisons are made during intervals when the convection was uniform and also when it was highly structured and variable. In addition to adding credence of the coherent scatter interpretation, such comparisons permit a rough assessment of the effects of spatio-temporal variability on incoherent scatter-based electric field measurements and of the potential contribution of fine structure to Joule heating.

* Corresponding author.
E-mail address: dlh37@cornell.edu (D.L. Hysell).

1364-6826/$ - see front matter © 2009 Elsevier Ltd. All rights reserved.
doi:10.1016/j.jastp.2008.10.013

2. Observations

Combined radar observations were made between January 11 and 26, February 7 and 13, and August 1 and 9, 2007, and again between January 12 and 20, 2008. Here, we focus on data from January 17, 2007, representing one of them most active events observed. The top panel of Fig. 1 shows the convection electric field derived from PFISR incoherent scatter radar observations. The vector drifts are plotted with respect to magnetic coordinates. The estimates are based on long-pulse F region line-of-sight Doppler shift measurements along seven PFISR pointing positions (see Table 1). Vector convection profiles versus magnetic latitude and time are estimated using a regularization procedure which assumes L-shell invariance (Heinselman and Nicolls, 2008). The fundamental time resolution of the PFISR data is about 11 s, but for this analysis, additional integration was performed to improve the statistics, yielding the plotted resolution of about 75 s. Statistical uncertainty remains significant beyond about 68° magnetic latitude.

The middle panel of Fig. 1 shows electron density profiles as a function of altitude measured with the PFISR. The data are derived from a 30 μs uncoded pulse experiment. They represent range corrected, normalized power but do not reflect a correction for nonunity T_e/T_i temperature ratios. The density data shown here have been integrated for 2 min. They are from beam 1 but are typical of all of the PFISR beams for this event. They depict precipitation-induced ionization with a peak that start near 120 km and moves slowly downward throughout the event. The

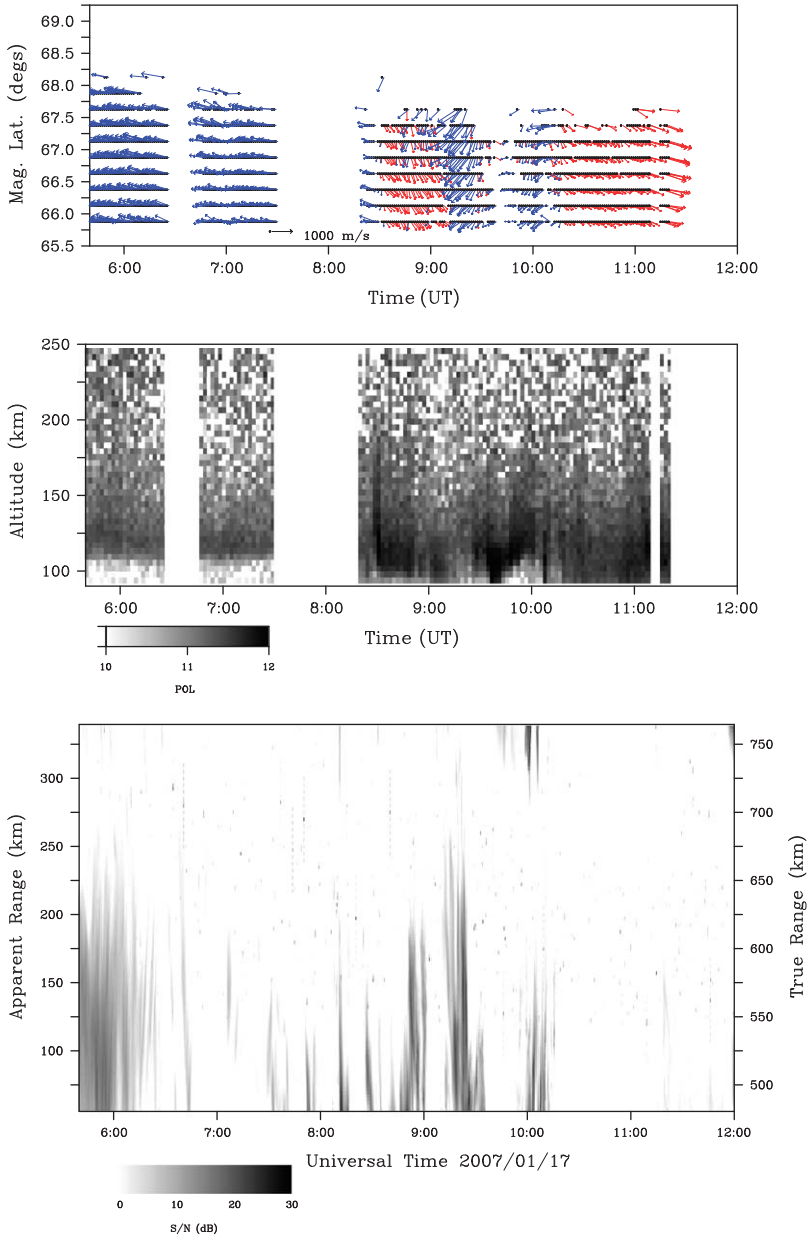

Fig. 1. Radar observations from January 17, 2007, made two days prior to the NASA JOULE II experiment. (top) Convection pattern estimated from PFISR long-pulse incoherent scatter data. Red and blue arrows denote westward and eastward flows, respectively. Velocity estimates with relative errors less than 25% and absolute errors less than 200 m/s are plotted. These thresholds mainly prevent data from above about 68° from being plotted. Gaps appear where rocket range operations interrupted data acquisition. (middle) Electron density estimates derived from 30 μs uncoded pulse incoherent scatter data acquired along beam 1. Units are number density m^{-3} on a logarithmic scale. (bottom) Range time intensity (RTI) plot of coherent scatter received by the 30 MHz imaging radar in Anchorage. Most of the auroral echoes are range aliased, and their true range is the apparent range shown here plus the 415 km interpulse period. The patch of echoes around 1000 UT with the most distant apparent ranges are not aliased.

Table 1
PFISR beam pointing positions and sample altitudes.

Beam no.	0	1	2	3	4	5	6
Azimuth (deg)	−35.09	−16.23	−1.51	76.09	57.23	42.51	−154.3
Elevation (deg)	66.19	58.68	45.84	66.19	58.68	45.84	77.5
h 3 (km)	166.55	163.2	153.18	166.55	163.2	153.18	168.95
h 4 (km)	199.47	193.94	178.99	199.47	193.94	178.99	204.08
h 5 (km)	232.38	224.67	204.8	232.38	224.67	204.8	239.2
h 6 (km)	265.29	255.4	230.6	265.29	255.4	230.6	274.32
h 7 (km)	298.21	286.13	256.42	298.21	286.13	256.42	309.44
h 8 (km)	331.12	316.87	282.23	331.12	316.87	282.23	344.56

The first three beams point west of the magnetic meridian, and the next three point east. Beam pairs 0 and 3, 1 and 4, and 2 and 5 are symmetric about the magnetic meridian. Beam 6 is directed toward magnetic zenith (not used here). The range gates for processed long-pulse data, converted to altitude, are also tabulated for gates 3–8 which are of primary interest here.

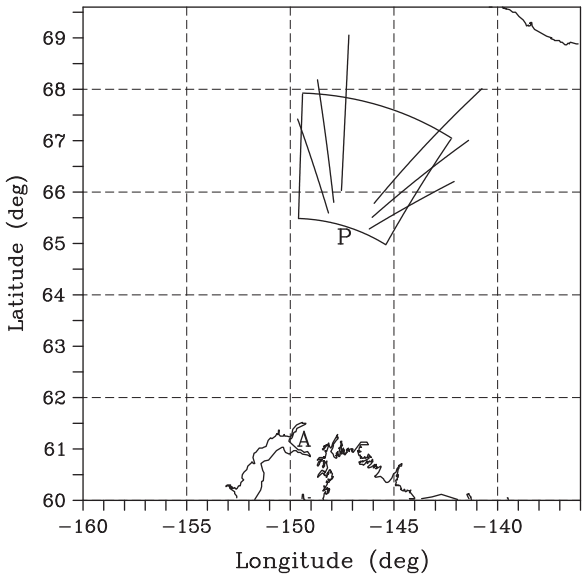

Fig. 2. Diagram comparing the regions observed by the 30 MHz coherent scatter radar in Anchorage (A) and the PFISR ISR at Poker Flat (P). The trapezoidal sector shows the field of view of the coherent scatter radar and is bounded by the beamwidth between first nulls (BWFN) of the transmitting antenna radiation pattern and the range gating. The six arcs represent samples taken along the six PFISR downrange pointing positions in the *F* region, mapped along geomagnetic field lines into the *E* region.

peak dipped and intensified between 0830 and 0900 UT and again between 0935 and 1000 UT, with the convection slowing drastically during the latter intensification.

The bottom panel of Fig. 1 shows coherent scatter radar data for the same time interval. These data were acquired by the 30 MHz imaging radar located at the High-Latitude Monitoring Station (HLMS) site in Anchorage operated by the Geophysical Institute. The radar observes backscatter from 5-m *E* region field-aligned plasma density irregularities. The range and time resolution of the data are 2.5 km and 3.5 s, respectively. The main beam of the 30 MHz radar is directed from Anchorage toward the PFRR at a geographic azimuth of 14°. The PFISR is therefore at the approximate center of the 30-MHz radar field of view and about 450 km downrange (see Fig. 2 for the geometry of the two radars and their overlapping observations). Radar range corresponds roughly to latitude, with the echoes shown here spanning latitudes between about 65° and 67° geographic (add ∼0.35° to convert to geomagnetic latitude). Note that all the auroral echoes except those near the top of the panel are range aliased and that their true range is the apparent range plus the 415 km radar interpulse period.

Auroral *E* region plasma irregularities are caused by Farley Buneman instabilities which occur when the electric field exceeds a threshold of about 20 mV/m in the ion frame of reference (see reviews by Haldoupis, 1989; Sahr and Fejer, 1996; Moorcroft, 2002). While large electric fields are necessary for *E* region coherent backscatter, they are not sufficient. Low *E* region plasma density, precipitation-driven absorption, and unfavorable propagation conditions can prevent strong echoes. Most often, however, coherent scatter echoes accompany ionospheric electric fields meeting the threshold condition. Coherent scatter was strongest around 0600 UT, when the convection was rapid (∼1300 m/s) and nearly westward, and again just after 0900 UT, when it was rapid (∼1200 m/s) and nearly southwestward. The convection reversed several times after 0800 UT.

Quantitative comparison between incoherent and coherent scatter radar data require the latter to be resolved in azimuth as well as range. Accordingly, spaced antenna techniques and statistical inverse theory are used to construct images from the 30 MHz coherent scatter multi-baseline interferometer data. Images for different Doppler spectral components can be computed separately and combined into a composite, representing the Doppler spectrum versus range and bearing. Images are constructed in three spatial dimensions, but the elevation dimension is noninformative for backscatter from field-aligned plasma irregularities and is integrated out, leaving two-dimensional images in azimuth and range. The particular imaging technique used here was reviewed recently by Hysell and Chau (2006). Characteristics of the 30 MHz radar in Anchorage were reviewed by Bahcivan et al. (2005). For these experiments, the range and time resolution is about 2.5 km and 3.5 s, respectively. Bahcivan et al. (2006) found an excellent correspondence between the radar images and conventional optical auroral imagery, with pronounced features in the former often occurring near the boundaries of optical auroral forms in the latter. (Unfortunately, clouds prevented optical observations throughout most of the night of January 17, 2007.)

Fig. 3 shows coherent scatter data for 0600 UT on January 17. The abscissa is the direction cosine of the radar wavevector with respect to the longest horizontal interferometry baseline. It can be regarded here as the sine of the azimuth angle relative to the direction of the main beam of the radar, which is directed at 14° geometric azimuth from Anchorage. Imaging radar data occupy the grid spanning 64 direction cosines and 96 range gates shown. The range resolution is 2.5 km, and the angle resolution is about 0.35°. The span of direction cosines represented in the figure matches the beamwidth between first nulls (BWFN) of the main antenna array. The two-way radiation pattern is reduced by 20 dB at direction cosines ±0.15, defining the effective width of the imaging field of view.

A complete Doppler spectrum is computed for each cell on the grid. Since the interpulse period is 415 km, Doppler velocities between ±900 m/s can be measured unambiguously. The first three moments of each spectrum are represented graphically, with the brightness, hue, and saturation of the pixel colors set according to the signal-to-noise ratio, Doppler shift, and spectral width of the backscatter, respectively. Bright pixels represent intense backscatter (spanning 6–30 dB SNR here). Blue (red) tones represent blue shifts (red shifts). Pure (pastel) colors denote narrow (wide) spectra. The data shown are mainly characterized by relatively small Doppler shifts and large spectral widths.

The empirical formulas used by Hysell et al. (2008) relating the spectral moments (Doppler shift and spectral width) to the

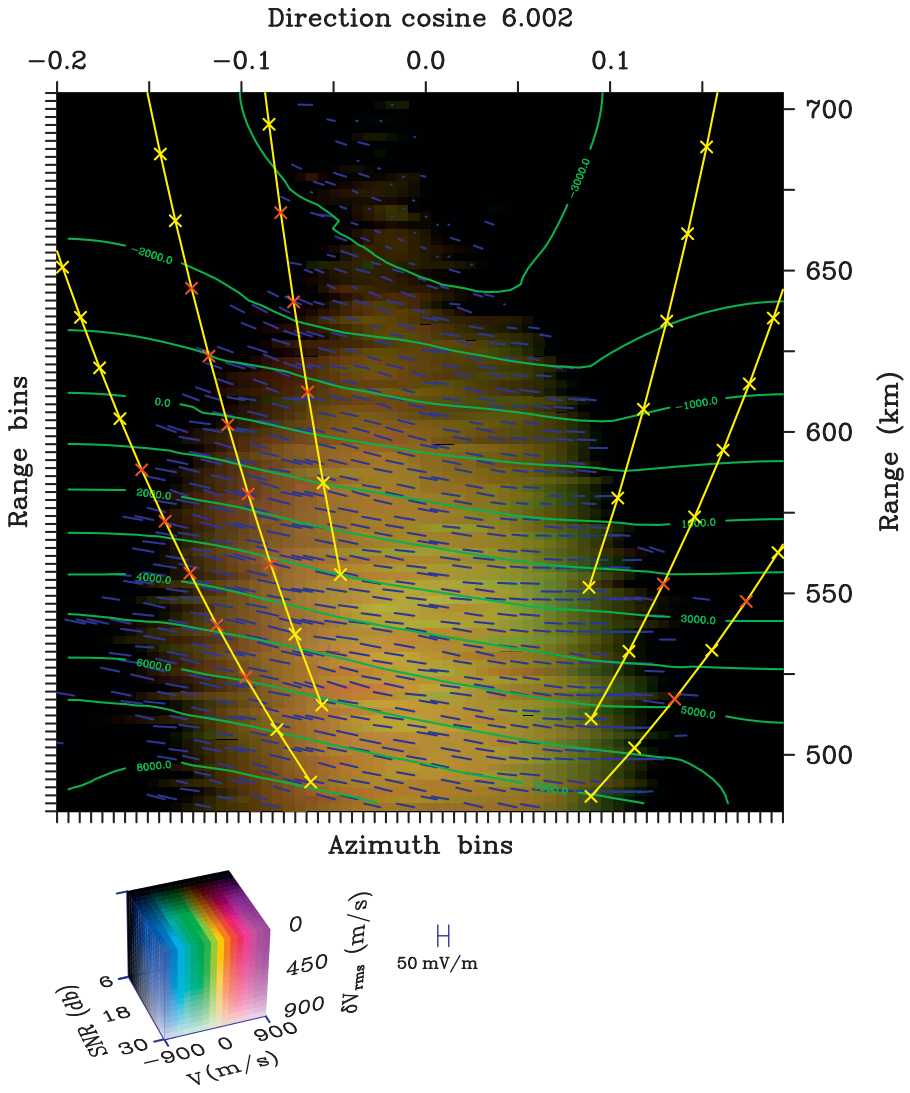

Fig. 3. Coherent scatter radar image of auroral *E* region plasma irregularities for January 17, 2007, 0600 UT. Backscatter features are plotted as a function of range and direction cosine with respect to the main horizontal radar interferometry baseline. The vertical bisector of the figure runs parallel to the radar main beam. The colors of the pixels that make up the image are assigned according to the moments of the Doppler spectrum in the given range/azimuth angle bin (see scale at lower left). The blue lines are estimates of the convection speed and direction derived from the spectral moments. Green contours are the estimated regional convection pattern found through regularization. Yellow lines trace six beams of the PFISR radar, mapped along geomagnetic field lines into the *E* region scattering volume. "×" symbols indicate the centers of the PFISR radar samples. Only PFISR samples taken from *F* region altitudes are used here. A red symbol signifies the presence of coherent scatter data nearby that can be used for comparison.

background electric field can be written as

$$\overline{\omega}/k = \hat{C}_s(V_d)\cos\theta + v \tag{1}$$

$$\delta\omega_{\rm rms}/k = \alpha\hat{C}_s(V_d)|\sin\theta| \tag{2}$$

where ω is the Doppler frequency, k is the radar scattering wavenumber, θ is the flow angle with respect to the radar line of sight, and v is the line-of-sight ion drift speed in the scattering volume, which is taken here to be the same as the neutral wind speed. The term $\hat{C}_s$ is the presumptive ion acoustic speed. According to Nielsen and Schlegel (1985) and Nielsen et al. (2002), this roughly obeys $\hat{C}_s \approx 400 + 1.1\times10^{-4}V_d^2$, where V_d is the $\mathbf{E}\times\mathbf{B}$ convection speed. (See also Robinson, 1986; St.-Maurice, 1990.) The dependence of $\hat{C}_s$ on V_d has been attributed quantitatively to wave heating associated with the parallel component of the wave electric field (St.-Maurice and Laher, 1985; Providakes et al., 1988; Milikh and Dimant, 2002, 2003; Bahcivan, 2007) and is ultimately what permits the estimation of the vector electric field from single-station observations using (1) and (2). Note that St.-Maurice et al. (1999) have shown that electron temperatures are surprisingly predictable functions of convection strength.

A recent numerical study of the Farley Buneman gradient drift (FBGD) instability by Oppenheim et al. (2008) provides theoretical support for (1) and (2). A heuristic interpretation was given by Hysell et al. (2008). In it, primary waves propagate nearly parallel to the convection velocity at or near the ion acoustic speed in the ion frame of reference, the threshold speed for linear instability. Driven beyond threshold, they generate a spectrum of secondary waves through nonlinear mode coupling. The combination of the primary and secondary waves produces patchy irregularities, and enhanced (coherent) backscatter results from the discreteness of the patches. The secondary waves limit the primary wave phase speeds through a combination of mode coupling, quasilinear effects, and wave heating, maintaining the condition of marginal stability.

The secondary waves are also FBGD in nature, excited by the polarization electric field of the primary but also modified by the density gradient of the primary, which has the effect of reducing the threshold speed (e.g. Farley and Fejer, 1975). At an arbitrary flow angle, the coherent scatter radar observes a mean Doppler shift related to the line-of-sight projection of the mean motion of the patchy irregularities, which are locked to the primary wave and behave like hard targets. This reasoning implies (1). Spectral broadening reflects the transverse motion of the patchy irregularities which alternates direction in different phases of the primary wave and which is limited in amplitude by the modified threshold speed as embodied in the α parameter above. This reasoning implies (2). Adapting Hamza and St.-Maurice (1993) and Hysell et al. (2008) gave a formal expression for the α parameter, but one that is impractical to evaluate. Experimentally, α was found to be of the order of $\frac{1}{4}$–$\frac{1}{2}$. In what follows, we set $\alpha = \frac{1}{2}$.

Although the PFISR can be used to measure lower thermospheric neutral wind speeds, results during this experiment were inconclusive. Our procedure for estimating the line-of-sight neutral wind speed at the *E* region scattering altitude is to use the smallest value of $|v|$ that prevents (1) and (2) from producing untenable results ($V_d^2 < 0$) anywhere or at any time in the event of interest. This is admittedly rather crude and, undoubtedly, a source of error. Drift velocities in Fig. 3 were computed assuming $v = 0$, affording reasonably good agreement with PFISR-measured convection nonetheless (see below).

Another unknown parameter in this inversion is the sign of the flow angle, which could vary across the image in principle. In view of the convection pattern shown in the top panel of Fig. 1, the sign was assumed to be everywhere consistent with westward (rather than eastward) flow.

The blue lines in Fig. 3 represent $\mathbf{E} \times \mathbf{B}$ drift velocities inferred from the coherent scatter spectra using (1) and (2). (Note that only a small fraction of the inferred vectors are plotted to keep the figure uncluttered.) In the coordinate system of the figure, radial and azimuthal vector components correspond to radar line-of-sight and transverse drifts, respectively.

The plotted vectors suggest strong westward convection with a small poleward component as seen in Fig. 1. While the directions of the vectors appear to vary from one side of the figure to another, this is really just a consequence of the figure's curvilinear coordinate system. In geographic coordinates, both the magnitude and direction of the drift velocity vectors are nearly uniform in space. Numerical calculations show that the inferred flow is essentially incompressible.

A model convection pattern was calculated and superimposed in Fig. 3, which shows model equipotential contours in green (in units of Volts). The pattern was calculated using statistical inverse methodology (e.g. Menke, 1984; Tarantola, 1987). A cost function was formulated including the model prediction error (the χ^2 discrepancy between the measured spectral moments and predictions based on the forward model (1) and (2)). The cost function also included a regularization parameter, the L2 norm of the predicted electric field. Minimizing the cost function produced the equipotentials shown, which are consistent with the measurements and also smooth and regular. Minimizing the model electric field outside the regions where we have data is a reasonable strategy since it is possible that the true electric field fell below threshold there. Even so, we do not attach much confidence to electric field estimates made in the absence of actual data. That a potential function could be found that is consistent with the inferred $\mathbf{E} \times \mathbf{B}$ drifts supports the plausibility of the coherent scatter data interpretation.

The yellow lines in Fig. 3 represent the six off-zenith (magnetic) beam pointing positions of the PFISR. Points along the beams have been mapped downward along geomagnetic field lines to the *E* region probed by the coherent scatter radar and then transformed into the coordinate system of the figure. "×" plotter symbols indicate the locations of the centers of the PFISR long-pulse mode processed data range gates. The nearest two range gates on each beam fall below the *F* region, and ISR data from them are not considered. A red plotter symbol is one for which nearby coherent scatter data exist. Refer to Table 1 for the PFISR beam pointing positions and long-pulse mode sample altitudes.

Where available, coherent scatter-derived vector drift estimates in the immediate vicinity of the PFISR processed data range gates are averaged, and the corresponding PFISR line-of-sight drifts predicted from them. The predictions, which include the appropriate geometric corrections, are then compared directly to measurements obtained through fitting the incoherent scatter autocorrelation functions. We can expect efficient mapping of perpendicular electric fields with the scale sizes in question here (at least several km) along magnetic field lines in view of the arguments first presented by Farley (1959, 1960). The PFISR long pulse is 480 μs (72 km) long, and processed line-of-sight drift estimates are produced at intervals half the length of the pulse (36 km). Range resolution is degraded somewhat by the summation rules applied in the long-pulse analysis and is effectively about 90 km. Ideally, the coherent scatter data should be averaged over elongated regions in Fig. 1 matching the long-pulse range resolution for the comparison. The limited coverage of the coherent scatter data generally makes this impractical, however. Discrepancies are expected to arise where spatial fine structure appears in the convection pattern. Temporal fine structure will be signified by fluctuations in the coherent scatter data occurring on timescales shorter than the incoherent scatter integration time. The analysis also neglects the contribution of parallel (to **B**) drifts to the line-of-sight ISR measurements, another potential source of discrepancy.

Line-of-sight long-pulse incoherent scatter drift measurements from the PFISR are compared with predictions derived from *E* region coherent scatter spectra in Fig. 4. Comparisons for six beams and six PFISR range gates are shown. West (east) beams are shown at left (right). The PFISR data are plotted as rectangles meant to convey the measurements and corresponding error bars. Coherent scatter predictions are plotted as points. Positive values denote drifts away from the PFISR. Large positive (small negative) drifts dominate the westward (eastward beams). Overall, the correspondence between the two datasets is close, with general trends and small perturbations being common to both. A few localized features in the coherent scatter drifts, for example in beam 2 between 610 and 0615 UT, are not very visible in the incoherent scatter data, suggesting that they may not have been spatially resolved by the ISR long pulse.

Because of the spatio-temporal uniformity of the convection, the homogeneity assumptions entering into the computation of the convection pattern in Fig. 1 appear to have been well justified, and the spatial resolution of the long-pulse experiment adequate for all intents and purposes. There is no significant discrepancy between that convection pattern and the one shown in Fig. 3. Both indicate a maximum convection speed of about 1300 m/s. In view of this uniformity, estimates of the Joule heating rate inferred from Fig. 1 would likely imply no significant underestimate due to neglected fine structure.

Fig. 5 shows a coherent scatter radar image for January 17, 2007, 0922 UT during the interval of strong southwestward convection indicated in Fig. 1. The backscatter intensity increased at this time to a peak of about 30 dB SNR, and the range spread of the echoes expanded to nearly fill the sample raster. The coherent scatter Doppler shifts in this example can be much larger than in the data from 0600 UT, exhibiting a maximum of about 700 m/s in the northeast quadrant. (Note that we refer here to the coherent

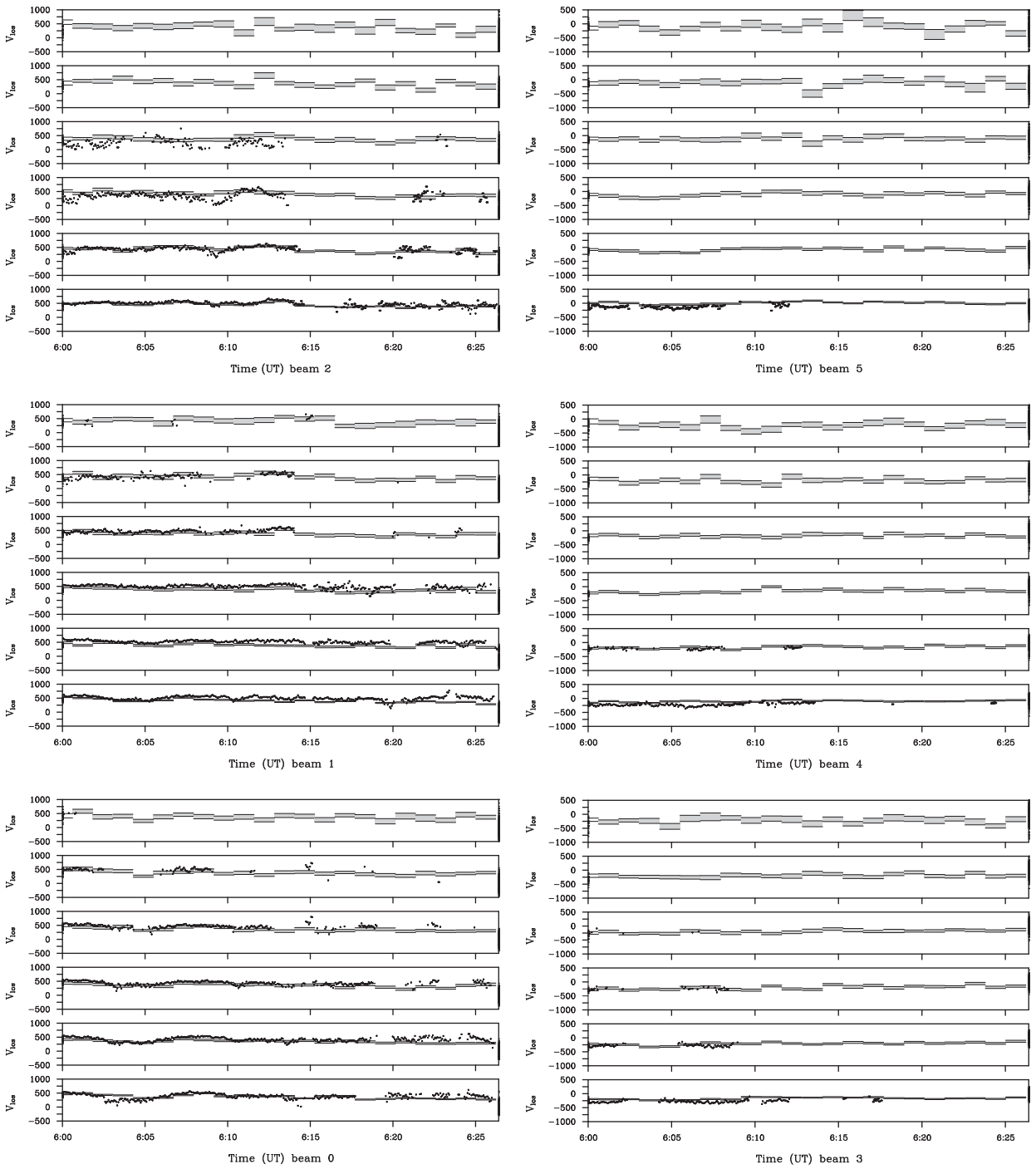

Fig. 4. Comparison of PFISR line-of-sight drifts (line plots) with values predicted on the basis of coherent scatter spectral moments (points). Positive values denote drifts away from the PFISR. Data for six beams and six range gates are shown. These data correspond to a period of uniform, constant flow.

scatter Doppler shift, as opposed to a convection speed.) The spectral widths are narrowest where the Doppler shifts are smallest, indicating small flow angles with respect to the radar line of sight.

Vector drifts were estimated according to (1) and (2) assuming a 150 m/s meridional neutral wind speed, the smallest figure that prevents ($V_d^2 < 0$) everywhere and that simultaneously affords the best agreement with incoherent scatter measurements made along the west PFISR beams (see below). Westward (as opposed to eastward) flow was again assumed. A convection pattern was also fit to the data using statistical inverse methods as above. The largest convection speeds implied by the figure are nearly 1800 m/s in the northeast quadrant. This is significantly larger than the largest values seen in Fig. 1. Fairly drastic variations in convection speed and direction are also evident throughout the figure. The variations have the form of bands reminiscent of banded layers that characterize radar aurora morphology.

The auroral echoes are concentrated on the left side of Fig. 5, affording considerable overlap with the west PFISR beams but very limited overlap with the east beams. Toward the west, coherent scatter-derived drifts remain relatively uniform and

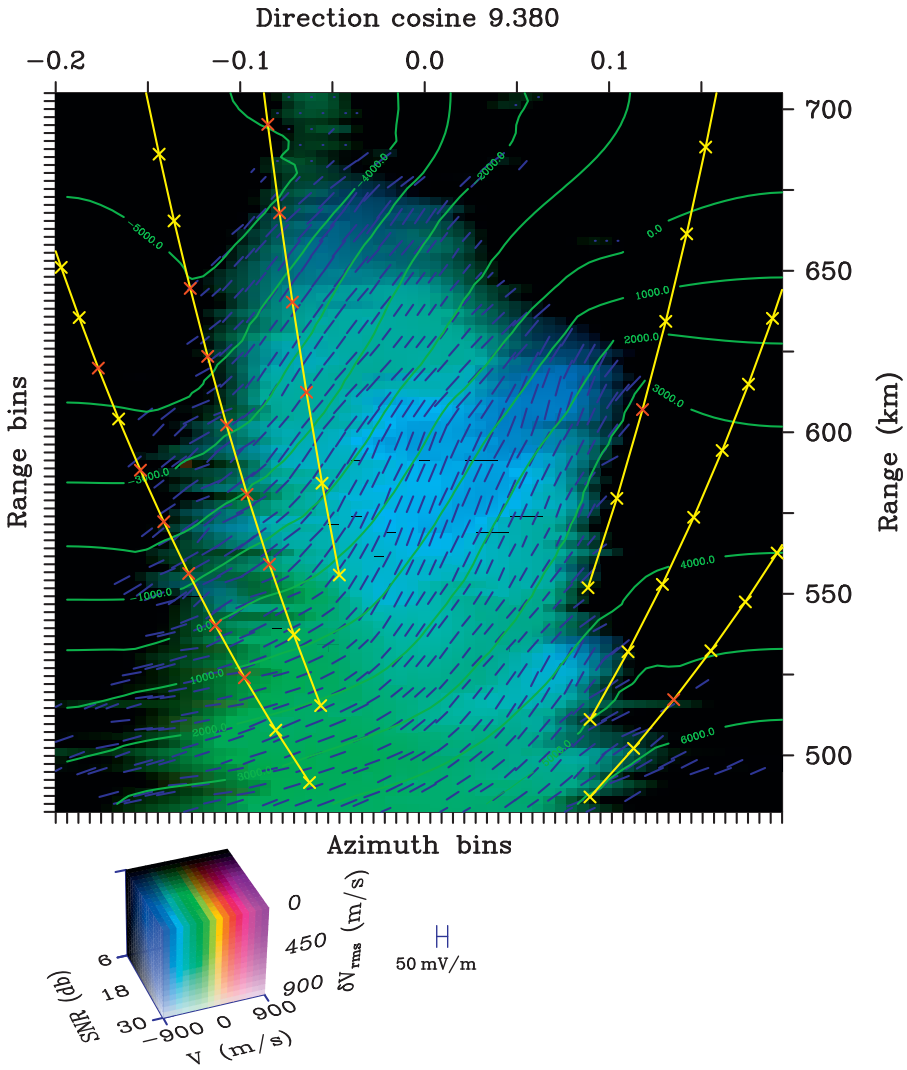

Fig. 5. Coherent scatter radar image of auroral *E* region plasma irregularities for January 17, 2007, 0922 UT. The electric field in this example contains much more spatial structure than the example in Fig. 2. Equipotential contours were estimated under the assumption of westward (rather than eastward) convection. This assumption is not well justified where the convection is close to parallel to the radar line of sight (see text).

constant between about 0912 and 0930 UT. This is not true toward the east, where distinct flow features comparable in size to the distance between the PFISR samples appear and disappear in the 30 MHz radar imagery. A ragged border on the right side of the scattering region, which fluctuates dramatically in time, delineates a zone further east where the electric field appears to fall abruptly below threshold. The electric fields probed by the east PFISR beams were therefore most likely highly irregular and inhomogeneous over the spatial dimensions spanned by the PFISR samples. The long-pulse mode had insufficient resolution to register all the structure in the line of sight flows in the east beams, which were themselves too widely spaced to sample all the important features in the flow. The *L*-shell invariance assumption underlying the estimation of a vector convection pattern from incoherent scatter measurements moreover seems to have been violated.

Fig. 6 shows a comparison of line-of-sight drifts measured by the PFISR with predictions based on coherent scatter-derived drifts like those shown in Fig. 5 for the period 0900–0930 UT. The format of the figure is identical to that of Fig. 4. Notice that the drifts measured along the west beams are uniformly small, particularly along beams 0 and 1. This is consistent with southwestward flow approximately normal to those beams and in agreement with the convection pattern shown in Fig. 5. The plotted points also indicate reasonable agreement between results derived from incoherent and coherent scatter. Discrepancies are larger and more frequent than in the data from 0600 UT when the convection was apparently more uniform and steady. In particular, a number of oscillations with a period of about 1 min are evident in the coherent scatter results but appear to be unresolved in the 75 s incoherent scatter time integrations. These could be signatures of micropulsations.

However, southwestward flow is not consistent with the line-of-sight PFISR drifts measured along beam 3, which are also small. Drifts increase in magnitude somewhat on beams 4 and 5, peaking at about −700 m/s between 0915 and 0920 on beam 5. Significant differences between line-of-sight drifts measured on the east PFISR beams (3, 4, and 5) indicate spatial inhomogeneity in the flow over the area spanned by the PFISR beams.

The line-of-sight drifts predicted by coherent scatter radar imagery show poor agreement with measurements along the east PFISR beams, the former having much larger magnitudes than the latter, particularly along beams 3 and 4. We attribute the discrepancy to inhomogeneity in the electric field on the east side of the volume shown in Fig. 5, which was likely coincident with discrete auroral forms in view of experience from previous

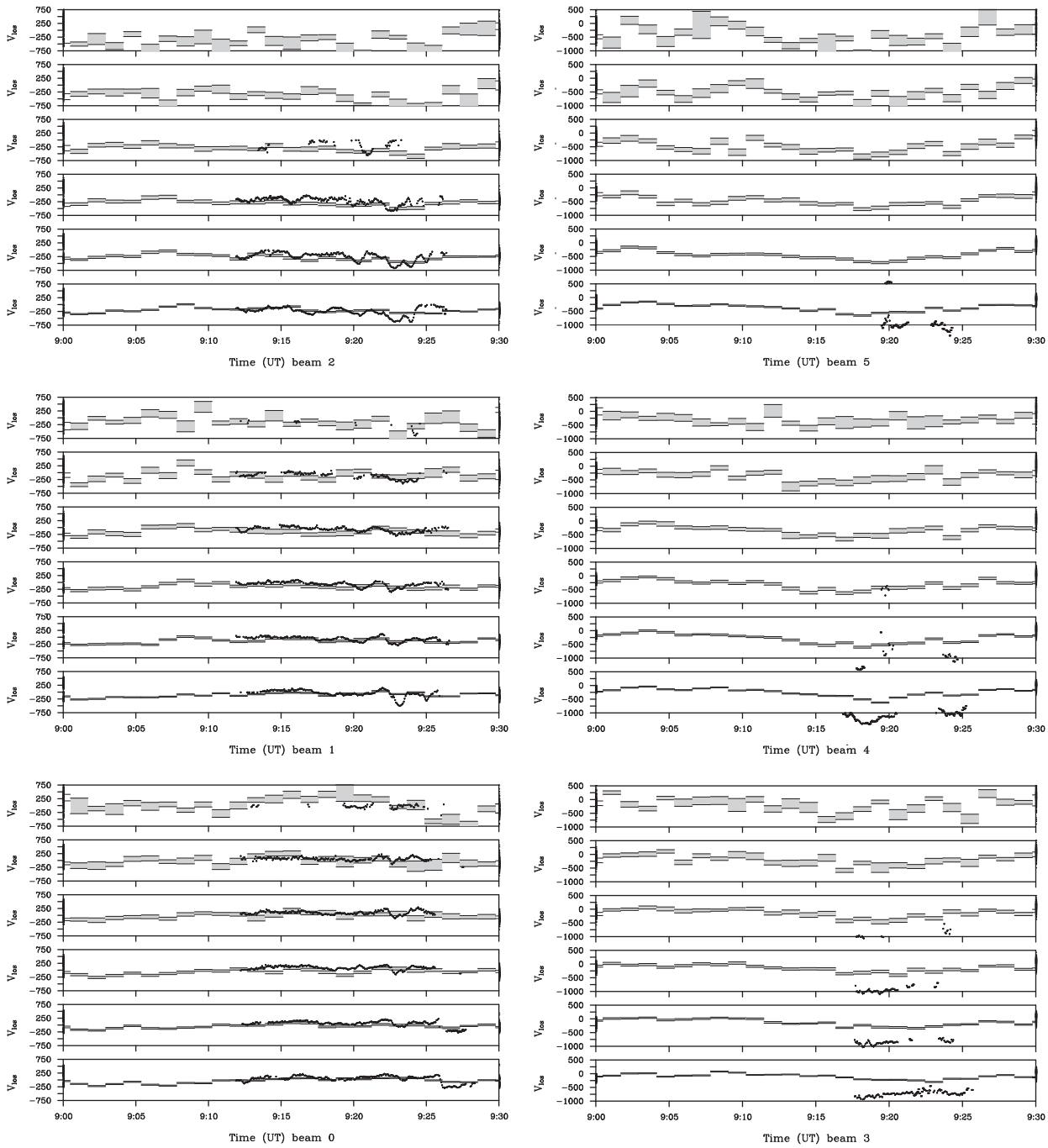

Fig. 6. Comparison of PFISR line-of-sight drifts (line plots) with values predicted on the basis of coherent scatter spectral moments (points). Positive values denote drifts away from the PFISR. Data for six beams and six range gates are shown. These data correspond to a period of irregular flow.

imaging experiments. The actual convection streamlines could well have resembled the equipotentials plotted in Fig. 5, which illustrate a way for the electric field to fall below threshold abruptly outside the scattering boundary by turning normally to the east beam directions. It is even possible that the zonal convection reversed in places and times under the east beams, something that would be invisible to the imaging radar but that could account for the small line-of-sight drifts measured there. In view of the inhomogeneity evident in the east side of Fig. 5 and the fact that coherent scatter arises selectively only from regions above threshold, it is not surprising that the imprecise averaging strategy necessitated by sparse coherent scatter data cannot reproduce the east beam incoherent scatter long-pulse drift measurements.

The average convection velocity across the radar illuminated volume in Fig. 5 is southwestward at about 1200 m/s. This is very close to the PFISR estimates for the same time. Despite evidence of unresolved flow variations across the volume spanned by the PFISR samples, gross inferences about the average convection drawn from those samples and combined using regularization do not depart significantly from gross inferences drawn from more finely resolved coherent scatter. Similar comments hold for the entire January 17 dataset. This attests to the robustness of the PFISR long-pulse data assimilation algorithm developed by

Heinselman and Nicolls (2008), even in the presence of unresolved fine structure.

3. Electric field variance

The coherent scatter radar imagery together with (1) and (2) form the basis for estimating the convection electric field over the 30 MHz radar illuminated volume. Variance in the electric field, $\langle|\mathbf{E}|^2\rangle - |\langle\mathbf{E}\rangle|^2$, points to fine structure with scale size roughly comparable to or smaller than the volume spanned by the PFISR samples and possibly neglected in Joule heating rate estimates derived from long-pulse incoherent scatter data. In this case, the outer scale in question is the size of the radar illuminated volume or about 200 km squared, and the inner scale is the pixel size, which is about two orders of magnitude smaller in both spatial dimensions.

Fig. 7 shows estimates of $\langle|\mathbf{E}|^2\rangle$ and $|\langle\mathbf{E}\rangle|^2$ computed from vector field estimates like those shown in Figs. 3 and 5. It also shows the ratio of the former to the latter (R) which is the variance, normalized to the square of the mean, plus 1. A value greater than unity signifies the relative contribution to Joule heating from fine structure in the pattern. The convection was assumed to be purely westward in both intervals. This assumption is well justified from 0600 to 0630 UT. It is not as well justified from 0912 to 0930 UT, when the convection may have reversed near the eastern boundary of the radar illuminated volume in places at times. The ratio is therefore potentially underestimated in this interval, although probably not significantly since any reversals are likely confined to small regions and time intervals.

The convection was uniform and steady throughout the interval from 0600 to 0630 UT. Consequently, the contribution of fine structure in the flow to the second moment of the electric field is relatively small. The ratio R is approximately 1.1 and never more than about 1.25. Spatial intermittency in the flow evidently did not contribute significantly to Joule heating in this case. The RMS electric field varies between 55 and 75 mV/m which is consistent with the PFISR estimates in Fig. 1.

Between 0912 and 0930, the RMS electric field varies between about 45 and 65 mV/m, which is also consistent with the PFISR estimates in Fig. 1. The electric field ratio R meanwhile averages about 1.2 and briefly achieves a maximum of 1.5. The increase is expected in view of the relatively structured flow observed throughout the interval. Despite the irregular flow evident in Fig. 5, however, the ratio remains confined to relatively small values (less than a doubling) throughout most of the interval. The electric fields estimated with kilometric spatial resolution evidently add constructively throughout the radar illuminated volume, and whatever small-scale structure is present makes relatively little contribution generally to the overall Joule heating rate. Furthermore, local maxima in the ratio seem to be collocated with local minima in the second moment, $\langle|\mathbf{E}|^2\rangle$, suggesting that the contribution of fine structure to the overall heating of the ionosphere is not very significant, at least on the spatial scales considered here.

4. Discussion

That electric field fine structure may contribute significantly to the net Joule heating at high latitudes has been suspected at least since the 1970s. Recently, efforts have been made to quantify the effects more carefully by using modeling studies and the limited data available. Estimates of the contribution of subgrid scale heating vary considerably, ranging from 33% (Codrescu et al., 1995) to as much as a factor of two (Li et al., 1998; Codrescu et al., 2000). Codrescu et al. (2000) pointed out that the characteristics of the small-scale variability in the high-latitude electric fields are not well known, and Chun et al. (1999) concluded that the lack of information about the contribution of small-scale fluctuations to the Joule heating is a significant problem.

Variability occurs on a variety of spatial scales and arises both from features in the convection pattern of magnetospheric origin and from conductivity variations in the ionosphere due to spatial gradients in precipitation, photochemistry, and ionospheric plasma waves and instabilities. The contribution to Joule heating due to intermediate- and small-scale fluctuations below the resolution limit of the ISRs, SuperDARN radars, and magnetometers remains to be explored in detail. In this study, we have used coherent scatter radar imagery of the radar aurora to investigate the contribution of fine structure in the electric field convection on spatial scales between about 2 and 200 km to the second moment of the electric field.

Since the plasma convection is incompressible, variations in it are associated with vorticity. Let us model the convection as a region of uniform vorticity $\omega\hat{b}$ within a radius r_0 surrounded by a field-free region for simplicity. The associated electric field in the vortex is $\mathbf{E} = -(\omega B/2)\mathbf{r}$ where $\hat{b}$ is the unit vector parallel to the geomagnetic field and $\mathbf{r}$ is the radial vector from the center of a vortex. The ratio R in some region of space containing the vortex

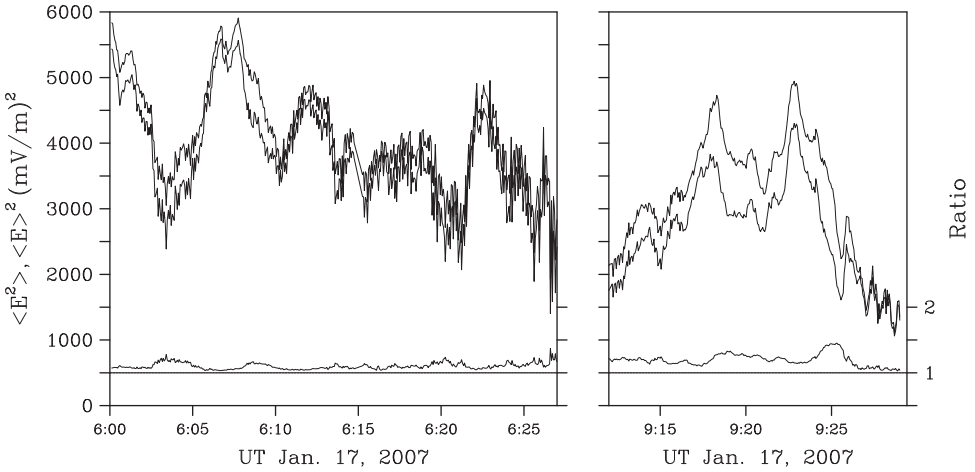

Fig. 7. Comparison of the mean squared and squared mean electric field estimated the coherent scatter radar images of the radio aurora. Note that the former is always greater than or equal to the latter. Results for steady and irregular auroral flows are shown at left and right, respectively. The ratio $R \equiv \langle|E|^2\rangle/|\langle E\rangle|^2$ is also shown. All available coherent scatter data were incorporated into this figure.

in whole or in part does not depend on the vorticity but only on the radius of the vortex compared to the size of the area. This can be shown through direct computation of $\langle|\mathbf{E}|^2\rangle$ and $|\langle\mathbf{E}\rangle|^2$ in the volume.

For an area with dimensions $l \times l$, the ratio for this model can be shown to be approximately $R = (\frac{9}{8})\mathrm{sinc}^{-2}(\theta/2)$, where θ is the angle of the arc on the circumference of the vortex contained in the area. This angle is given roughly by $\theta/2 = \sin^{-1}(l/2r_0)$. The ratio in question can be arbitrarily large to the extent the area is large enough to contain a complete vortex ($\theta = 2\pi$), a situation for which the average electric field is zero. An area large enough to contain just a quadrant of the vortex ($l = r_0$) implies a ratio of about $R = 1.5$ or about the maximum value found in the analysis leading to Fig. 7. This situation is essentially what is shown in Fig. 5, one of the most contorted convection patterns radar imaging has produced. Still smaller areas (or, equivalently, larger vortices) entail smaller ratios. In Fig. 3, the radius of curvature of the convection is much larger than the area being analyzed, and the ratio R is consequently close to unity.

Since the $\sim 200 \times 200$ km area probed by the imaging radar seldom shows more than about a quadrant of a convection vortex, the ratio R for that area is seldom more than about 1.5. This means that errors in Joule heating rate estimates derived from the data associated with fine structure with scale sizes between about 2 and 200 km will be modest. Highly contorted electric fields accompany discrete auroral arcs in the radar images, but these are usually confined to small regions of space, so the contribution to net Joule heating could remain small.

Similar remarks must hold for analyses based on PFISR line-of-sight drifts, which are calculated on the basis of backscatter sampled across a comparably sized area. While fine structure with scale size less than a few hundred km is invisible to PFISR long-pulse experiments, this does not seem to seriously degrade the accuracy of average convection electric field estimates derived using the regularization method of Heinselman and Nicolls (2008).

The coherent scatter data treatment used here suffers from a number of limitations. The practical difficulty in measuring the width of a narrow spectrum translates into difficulty measuring small flow angles accurately. Since the sign of the flow angle cannot be determined, convection reversals and very small vortices accompanying them are moreover invisible to the imaging radar. This implies a potential overestimate in the average electric field across the radar illuminated volume and a corresponding underestimate of the electric field variance. Of course, strong convection leading to Farley Buneman waves is required in order for the measurement to be made at all, and our inability to estimate convection with the method routinely prohibits a truly systematic study.

The empirical formulas underlying this analysis are blunt instruments with only limited theoretical support, although the effects of wave heating have been quantified with varying degrees of rigor (Milikh and Dimant, 2002, 2003; Bahcivan, 2007). Numerical simulations of the FBGD instability by Oppenheim et al. (2008) confirm the quadrature behavior of the Doppler shift and spectral width of backscatter from auroral irregularities, but the physical significance of the α parameter and the physics surrounding phase speed saturation near the ion acoustic speed are not well understood. The analysis here rests upon a number of assumptions and neglects thermal effects, which tend to turn the propagation direction of Farley Buneman waves from the convection direction, and also the possible effects of conductivity gradients, which could invalidate the applicability of the empirical formulas in the vicinity of auroral forms. The handling of the effects of neutral winds in the absence of actual measurements is not very satisfactory but could be improved, for example, by incorporating the parameter into the inversion, solving for the wind that minimizes the global compressibility of the estimated flow vectors. More comprehensive analysis including temperature and wind profile measurements from the ISR, aspect sensitivity measurements from the coherent scatter radar, and optical support should help resolve many of these issues.

Acknowledgments

D.L.H. is grateful to J. Kelly and SRI International for hosting him as a Visiting Fellow during the completion of this work. D.L.H. is also grateful for the assistance of Mr. John Peters at the HLMS station operated by the Geophysical Institute of the University of Alaska, Fairbanks. The research was supported by award no. ATM-0531683 from the National Science Foundation and no. NNG05WC42G from the National Aeronautics and Space Administration to Cornell University and by award no. ATM-0541593 from the National Science Foundation and no. NNG05WC40G from the National Aeronautics and Space Administration to Clemson University. The PFISR was developed under NSF cooperative agreement ATM-0121483, and the data collection and analysis was supported under NSF cooperative agreement ATM-0608577.

References

Bahcivan, H., 2007. Plasma wave heating during extreme electric fields in the high-latitude *E* region. Geophys. Res. Lett. 34, L15106.

Bahcivan, H., Hysell, D.L., Larsen, M.F., Pfaff, R.F., 2005. 30 MHz imaging radar observations of auroral irregularities during the JOULE campaign. J. Geophys. Res. 110, A05307.

Bahcivan, H., Hysell, D.L., Lummerzheim, D., Larsen, M.F., Pfaff, R.F., 2006. Observations of collocated optical and radar auroras. J. Geophys. Res. 111, A12308.

Chun, F.K., Knipp, D.J., McHarg, M.G., Lu, G., Emery, B.A., Vennerstrøm, S., Troshichev, O.A., 1999. Polar cap index as a proxy for hemispheric Joule heating. Geophys. Res. Lett. 26, 1101.

Codrescu, M.V., Fuller-Rowell, T., Foster, J., 1995. On the importance of *E*-field variability for Joule heating in the high-latitude thermosphere. Geophys. Res. Lett. 22, 2393–2396.

Codrescu, M.V., Fuller-Rowell, T.J., Foster, J.C., Holt, J.M., Cariglia, S.J., 2000. Electric field variability associated with the Millstone Hill electric field model. J. Geophys. Res. 105, 5265.

Farley, D.T., 1959. A theory of electrostatic fields in a horizontally stratified ionosphere subject to a vertical magnetic field. J. Geophys. Res. 64, 1225.

Farley, D.T., 1960. A theory of electrostatic fields in the ionosphere at nonpolar geomagnetic latitudes. J. Geophys. Res. 65, 869.

Farley, D.T., Fejer, B.G., 1975. The effect of the gradient drift term on the type 1 electrojet irregularities. J. Geophys. Res. 80, 3087.

Haldoupis, C., 1989. A review on radio studies of auroral *E*-region ionospheric irregularities. Ann. Geophys. 7, 239–258.

Hamza, A.M., St.-Maurice, J.P., 1993. A turbulent theoretical framework for the study of current-driven *E* region irregularities at high latitudes: basic derivations and application to gradient-free situations. J. Geophys. Res. 98, 11,587–11,599.

Heinselman, C.J., Nicolls, M.J., 2008. A Bayesian approach to electric field and *E*-region neutral wind estimation with the Poker Flat Advanced Modular Incoherent Scatter Radar. Radio Sci. 43, RS5013, doi:10.10.29/2007RS003805.

Hysell, D.L., Chau, J.L., 2006. Optimal aperture synthesis radar imaging. Radio Sci. 41, RS2003.

Hysell, D.L., Michhue, G., Larsen, M.F., Pfaff, R., Nicolls, M., Heinselman, C., Bahcivan, H., 2008. Imaging radar observations of Farley Buneman waves during the JOULE II experiment. Ann. Geophys. 26, 1837–1850.

Li, F., Killeen, T.L., Burns, A.G., Wang, W., Roble, Q.W.R., Frank, L.A., Siywarth, J.B., 1998. Modeling of high-latitude thermosphere Joule heating at high spatial/temporal resolution (abstract). In: Eos Transactions on AGU, Spring Meeting Supplement, p. S32.

Menke, W., 1984. Geophysical Data Analysis: Discrete Inverse Theory. Academic, New York.

Milikh, G.M., Dimant, Y.S., 2002. Kinetic model of electron heating by turbulent electric field in the *E* region. Geophys. Res. Lett. 29 (12), 1575–1578.

Milikh, G.M., Dimant, Y.S., 2003. Model of anomalous electron heating in the *E* region: detailed numerical modeling. J. Geophys. Res. 108, 1350.

Moorcroft, D.R., 2002. Outstanding issues in the theory of radar aurora: evidence from the frequency dependence of spectral characteristics. J. Geophys. Res. 107.

Nielsen, E., Schlegel, K., 1985. Coherent radar Doppler measurements and their relationship to the ionospheric electron drift velocity. J. Geophys. Res. 90, 3498–3504.

Nielsen, E., del Pazo, F., Williams, P.J.S., 2002. VHF coherent radar signals from the *E* region ionosphere and the relationship to electron drift velocity and ion-acoustic velocity. J. Geophys. Res. 107.

Oppenheim, M.M., Dimant, Y., Dyrud, L., 2008. Large scale simulations of 2D fully kinetic Farley Buneman turbulence. Ann. Geophys. 26, 543–553.

Providakes, J.F., Farley, D.T., Fejer, B.G., Sahr, J., Swartz, W.E., Häggström, I., Hedburg, A., Nordling, J.A., 1988. Observations of auroral *E*-region plasma waves and electron heating with EISCAT and a VHF radar interferometer. J. Atmos. Terr. Phys. 50, 339.

Robinson, R.T., 1986. Towards a self consistent nonlinear theory of radar auroral backscatter. J. Atmos. Terr. Phys. 48, 417–422.

Sahr, J.D., Fejer, B.G., 1996. Auroral electrojet plasma irregularity theory and experiment: a critical review of present understanding and future directions. J. Geophys. Res. 101, 26,893–26,909.

St.-Maurice, J.P., 1990. Electron heating by plasma waves in the high-latitude *E* region ionosphere and related effects: theory. Adv. Space Res. 10, 239–249.

St.-Maurice, J.P., Laher, R., 1985. Are observed broadband plasma wave amplitudes large enough to explain the enhanced electron temperatures of the high-latitude *E* region. J. Geophys. Res. 90, 2843.

St.-Maurice, J.P., Cussenot, C., Kofman, W., 1999. On the usefulness of *E* region electron temperatures and lower *F* region ion temperatures for the extraction of thermospheric parameters: a case study. Ann. Geophys. 17, 1182–1198.

Tarantola, A., 1987. Inverse Theory. Elsevier, New York.